Electronic Supplementary Material (ESI) for Physical Chemistry Chemical Physics.
This journal is © the Owner Societies 2019

Supplementary Information

Supplementary Information

Received 00th January 20xx,
Accepted 00th January 20xx

DOI: 10.1039/x0xx00000x

Neutron Reflectometry to Measure in-situ the Rate Determining Step of Lithium Ion Transport through Thin Silicon Layers and Interfaces

Erwin Hüger,*[a] Jochen Stahn,[b] Paul Heitjans[c] and Harald Schmidt[a,d]

Content:

1. Literature survey

The main article presents neutron reflectometry (NR) measurements recorded during Li permeation (i.e., in-situ experiments) that allow the determination of the rate determining step of Li transport through thin Si layers and their interfaces to an oxide material. The methodology to measure Li transport through thin layers and their interfaces to solid-state Li reservoirs was introduced in reference [S1]. There, ex-situ NR investigations to measure Li permeation through 15 nm thin Si layers deposited adjacent to $LiNbO_3$ layers were described. Ex-situ means that annealing necessary to initiate the Li permeation process was stopped and the sample was cooled to room temperature for the recording of the NR pattern. Reference [S2] presents ex-situ NR and Secondary Ion Mass Spectrometry (SIMS) measurements showing that the same results were obtained by both methods. Obviously SIMS can be performed only ex-situ. Reference [S3] and [S4] exemplarily shows that in-situ measurement of Li permeation is feasible with NR. This was shown for amorphous Si layers with 5 nm thickness [S3] and for amorphous lithium silicide layers with 8.5 nm thickness [S4]. The bottleneck process for the Li permeation process through interfaces and thin silicon [S3] and lithium silicide [S4] layers adjacent to thin $LiNbO_3$ layers was not investigated in reference [S3] and [S4] because only one Si and only one lithium silicide layer thickness was studied. A detailed description of how Li permeability, diffusivity and solubility can be measured in 95 nm thick Si layers by SIMS depth profiling is reported in reference [S5]. There, it is shown that the knowledge of Li permeabilities is important for the understanding of lithium-ion battery (LIB) operation. I.e., reference [S5] gives a discussion of how the Li transport parameters help to understand the electrochemical storage of Li (lithiation process) in amorphous silicon. The measured Li permeation parameters contributed to explain why

---

[a] AG Mikrokinetik, Institut für Metallurgie, TU Clausthal, Clausthal-Zellerfeld, D-38678, Germany.

E-Mail: erwin.hueger@tu-clausthal.de

[b] Laboratory for Neutron Scattering and Imaging, Paul Scherrer Institut, Villigen, CH-5232, Switzerland.
[c] Institut für Physikalische Chemie und Elektrochemie, and ZFM – Zentrum für Festkörperchemie und Neue Materialien, Leibniz Universität Hannover, D-30167 Hannover, Germany.
[d] Clausthaler Zentrum für Materialtechnik, Technische Universität Clausthal, Clausthal-Zellerfeld, D-38678, Germany
See DOI: 10.1039/x0xx00000x

electrochemical lithiation of Si electrodes in LIB can take place by a moving phase boundary separating a high lithiated Li-Si phase from a poor or un-lithiated Si phase [S5]. The aim of reference [S6] was to compare Li permeation through chromium, carbon and silicon layers. NR and SIMS were applied ex-situ. Li permeation through carbon layers was found to be faster than through chromium layers and the latter to be faster than through silicon layers. It was not possible to determine Li permeability in Si from the experiments presented in reference [S6]. Finally, reference [S7] presents a SIMS depth profile study on the Li permeation process through 12 to 95 nm thin Si layers from which the rate determining step of Li transport through Si layers and the Si/LiNbO3 interface could be determined. The rate determining step was found to be the Li permeation process inside the Si material. As mentioned, SIMS depth profiling is performed destructively and ex-situ. On this issue, reference [S6] clearly demonstrates (by a comparison between SIMS and NR investigations) that the destructive nature of SIMS depth profiling methodology influences drastically the (measured) Li isotope concentration from which Li permeation is traced back (see the Supporting Information (SI) of reference [S6] and section 4 of the Supporting Information of the present work). The SI of reference [S6] shows that the real isotope and element distribution in the MLs is obtained by depth profiling with the non-destructive methodology of neutron scattering (neutron reflectometry). So, non-destructive methodologies, such as NR, are preferable for Li permeation measurements. This work presents in-situ and non-destructive measurements performed by the new methodology of focusing NR to elucidate the rate controlling step for the Li permeation process through thin silicon layers adjacent to thin $LiNbO_3$ layers.

2. Multilayer deposition and measurement techniques

Multilayers (MLs) of five [Si / $^7LiNbO_3$ / Si / $^6LiNbO_3$] units (see Figure S1b) were deposited on 0.65 mm thin silicon wafers using an ion-beam depositing set-up (IBC 681, Gatan, Pleasanton, CA, USA) [S8]. The Li isotope reservoir layers were sputtered from $^6LiNbO_3$ and $^7LiNbO_3$ targets with a ^6Li isotope enrichment of 95% and 7.5%, respectively. To protect the multilayer system from environment, an additional $^6LiNbO_3$ layer was deposited on top. For multilayer deposition, Si wafer substrates with lateral sizes of 5×10 mm^2 were used. Sputtering is accomplished by two Penning ion guns at an incident angle of 45°, positioned about 10 cm above the sample. Different target materials can be selected without breaking the vacuum. The $^6LiNbO_3$ and $^7LiNbO_3$ sputter targets were prepared by solid state syntheses as described in reference [S9]. The Si sputter target was purchased from Alfa Aesar (99.999%). The base pressure of the vacuum chamber was 5×10^{-7} mbar. Sputtering was done with Ar^+ ions at a working pressure of 5×10^{-5} mbar. The ion beam acceleration voltage was 5 kV and the ion beam current was 180 µA. During deposition, the specimen is rotated (30 rotations per minute) and rocked (rock angle: 30° and rock speed: 12° per second) to ensure a more uniform coating of the samples. Li transport through Si layers was induced by annealing the ML arrangement in Ar gas environment at temperatures up to 500 °C (773 K) for short times using a rapid thermal annealing oven (AO500, MBE Components, Germany).

Neutron reflectometry (NR) measurements were performed at the time-of-flight reflectometer Amor with the Selene focusing setup as described in the main article.

SIMS was done in depth-profiling mode, using a Cameca IMS 3f/4f machine. An O_2^+ primary ion beam (5 keV, ~50 nA) was used. Positive secondary ions were analyzed. Lithium has a high ionization cross section for positive ions. Hence, the Li^+ SIMS signal is of very high intensity. From the sputtered area of about 250 µm × 250 µm, the signal resulting from an area of 60 µm × 60 µm in the center was used for further processing in order to exclude crater edge effects. The measurements were performed at room temperature. Optical microscopy of SIMS craters was performed with a ZEISS AXIO ImagerM2m light microscope.

X-ray Reflectometry (XRR) was used to determine the layer thickness and to check the chemical contrast in the deposited multilayers. The X-ray measurements were performed with a Bruker D5000 diffractometer using CoK_α radiation and a scintillation counter detector. Reflectivity simulations were done with the Parratt32 software package (based on Parratt's recursion algorithm) [S10] and the scattering length density was calculated with the online calculator given in reference [S11].

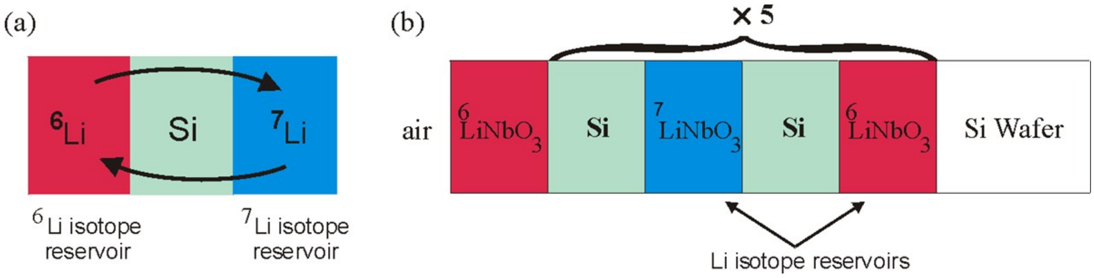

Figure S1. (a) Basic principle of an arrangement to measure Li permeabilities: a Si layer embedded between two Li isotope reservoir layers. (b) Sketch of MLs used for Li permeation experiments. A multilayer of five [Si/^{7}LiNbO$_3$/Si/^{6}LiNbO$_3$] units deposited on Si wafer and capped by a ^{6}LiNbO$_3$ layer.

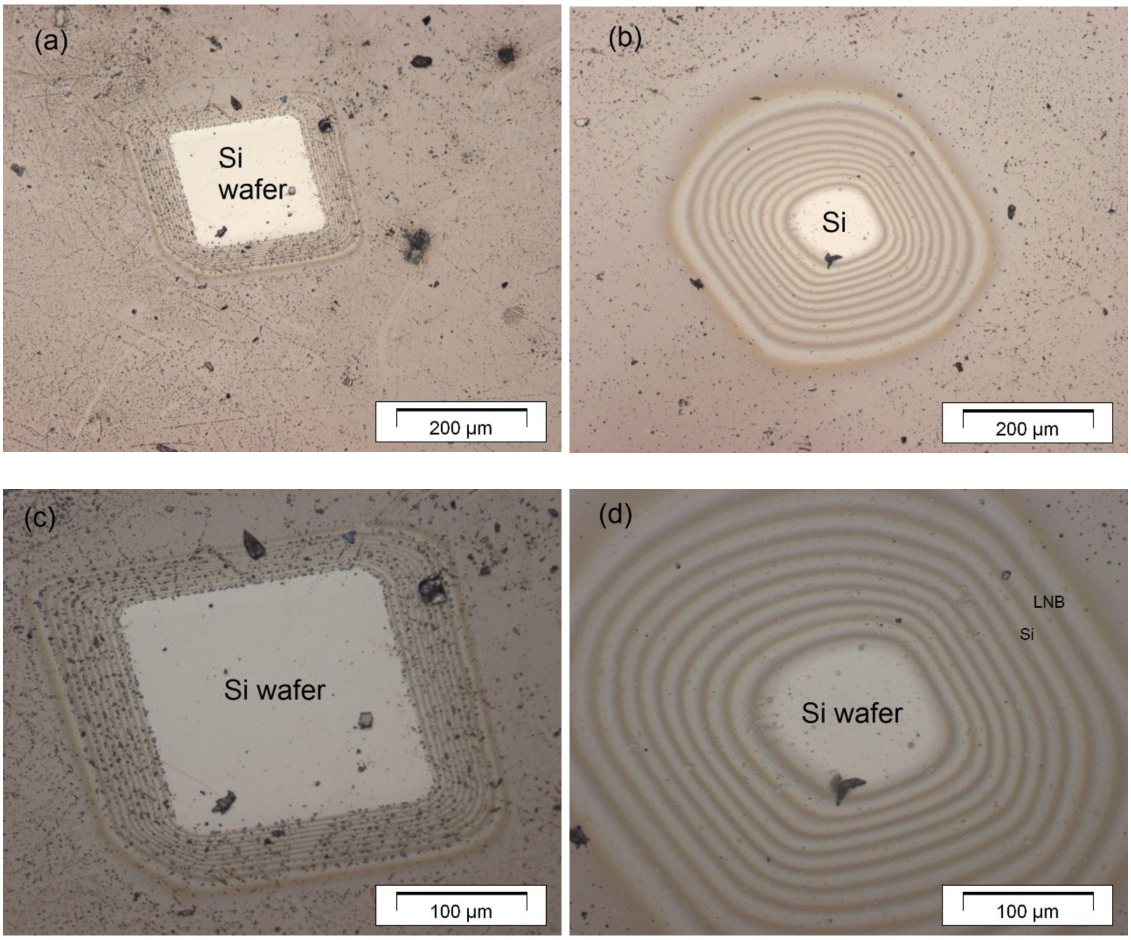

Figure S2. Light microscopy images for the visualization of the ML structure. Images of craters obtained by SIMS depth-profile of the ML with 22 nm thin Si intermediary layers. The crater bottom (silicon wafer) is the white region in the middle of the images. The bands located at the crater edge correspond to the LiNbO$_3$/Si multilayer structure. The darker bands are formed by dust accumulated at the position of the LiNbO$_3$ layers. (a,c) Crater obtained by a focused primary ion beam. (b,d) Crater obtained by a defocused primary ion beam for a better visualization of the bands located at the crater edge. (c.d) Enlarged view of the SIMS craters.

3. Microscopy on multilayers

The stratigraphic sequence of the multilayer (ML) stack is visualized in Figure S2 by images of craters obtained after SIMS depth profiling. An image contrast as bands is observed at the edge of the SIMS craters. This structure appears due to the interplay of the low-angle (oblique) SIMS crater edge and the layered arrangement of the multilayer. The crater which is visualized in Figure S2 (b,d) was obtained with the help of an defocussed primary ion beam resulting in a wider SIMS crater edge. The SIMS crater edge possesses a width of 50 microns in Figure S2 (a,c) and of 200 microns in Figure S2 (b,d). Hence, the SIMS crater edge cuts the 310 nm thin multilayer with a low slope (oblique) across a width of 50 (Figure S2 (a,c)) or 200 microns (Figure S2 (b,d)). Consequently, the low-angle cut of each (up to 22 nm) thin layers becomes visible over several µm large distances. The top view images visualize the material contrast of exactly this micrometer sized cutting edges of individual thin layers of the ML. The darker bands in Figure S2 correspond to

$LiNbO_3$ layers and the lighter bands to Si layers. The top view light microscopy of craters obtained during SIMS depth profiling enables the visualization of ML possessing individual layers thinner than the half of the light wavelength.

4. Layer thickness determination by X-ray reflectometry

Figure S3 presents the analysis of the XRR study. The Kiessig analysis (see the supporting information of reference [S5]) determines a double layer thickness (i.e., the thickness of the Si and $LiNbO_3$ layer) of (24 ± 0.1) nm, (28 ± 0.2) nm and (30 ± 0.2) nm. The results agree well with that obtained from neutron reflectometry analysis. The individual layer thicknesses for all samples were obtained from exhaustive NR analysis and are listed in Table S3 and S4.

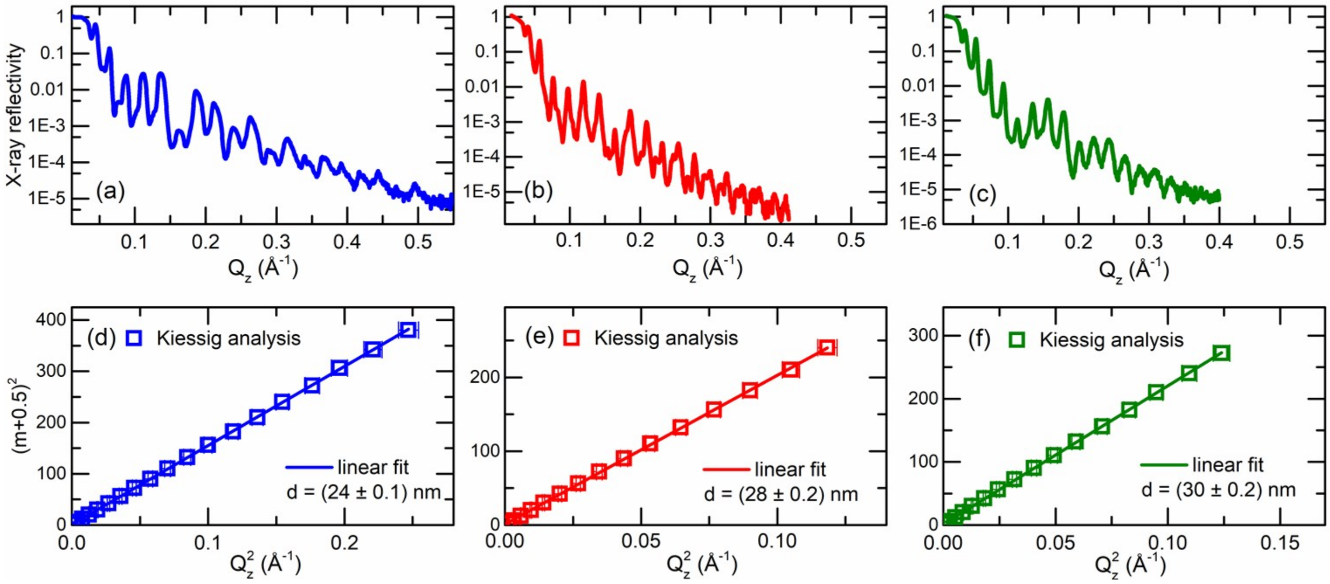

Figure S3. XRR pattern (a,b,c) and Kiessig analysis (d,e,f) of the XRR measurements of as-deposited MLs investigated in this work.

5. Secondary ion mass spectrometry data

Figure S4 presents element and isotope depth profiles recorded with secondary ion mass spectrometry (SIMS) on as-deposited MLs with 14, 17 and 22 nm thin intermediary Si layers. There are strong modulations in the element and isotope depth profiles as expected from the ML arrangement. The depth profiles show a double peak structure (see for example the Si depth profile) (Figure S4a,b,e,f,i,j). In contrast, the Li isotope fractions are not double peaked (Figure S4c,d,g,h,k,l). The depth profiles of the neutron scattering length densities (Figure 1 of the main article) also does not show a double peak structure. This indicates that the double-peak structure is produced by the influence of the ion beam sputtering process on the SIMS depth profile, preferably the matrix effect. Detailed neutron reflectometry (NR) simulations including the model for a double peak structure were performed in the SI of reference [S6] (Figure S12, S13 and S14 in SI of reference [S6]). They show that NR is capable of detecting a double peak structure if such a structure is present in the ML. The double peak structure would strongly reduce the intensity of the Bragg peak corresponding to the chemical contrast in the ML. The NR study demonstrates that the double peak signal is not present in the ML. The measured double peak SIMS depth profile has to appear due to the specific (destructive, charged particles) SIMS depth profiling methodology. I.e., the double peak signals in the SIMS depth profiles are produced by the SIMS measurement themselves. Summarizing this issue, (i) the SIMS depth profile does not correspond exactly to the real isotope and element distribution in MLs due to peculiarities of the SIMS measurement technique and (ii) the real isotope and element distribution in the MLs is obtained by depth profiling with the non-destructive methodology of neutron reflectometry. Therefore, the present study applies in-situ NR to elucidate the rate determining step for Li transport across thin Si layers and interfaces.

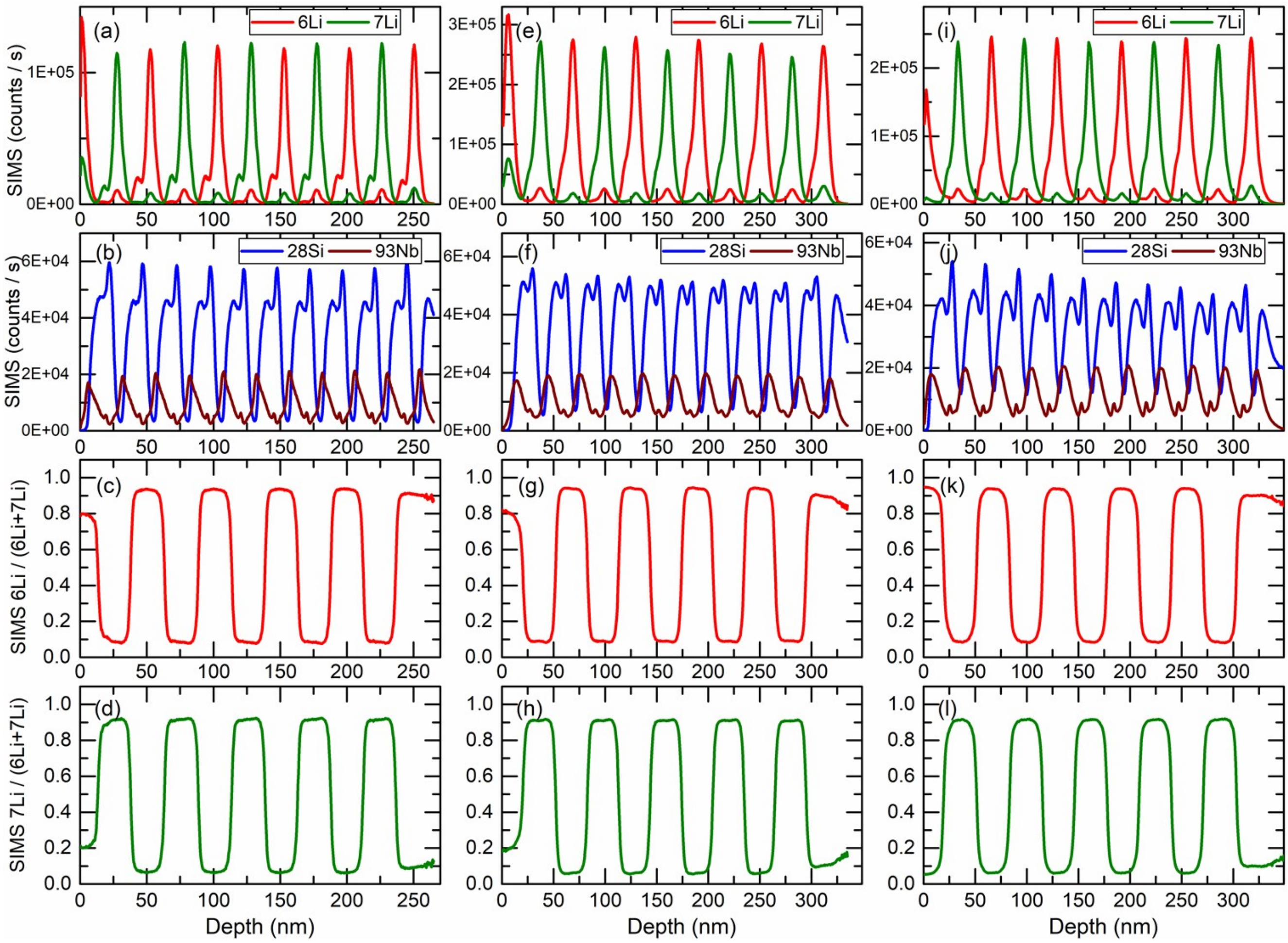

Figure S4. SIMS depth profiles for as-deposited MLs with (a-d) 14 nm, (e-h) 17 nm and (i-l) 22 nm thin Si intermediary layers. The thickness of $LiNbO_3$ layers were for (a-d) 10 nm, (e-h) 10 nm and (i-l) 8 nm. Depicted are depth profiles for ^{6}Li and ^{7}Li (a,e,i), ^{28}Si and ^{93}Nb (b,f,j) SIMS signals. (c,g,k) Depth of ^{6}Li fraction and (d,h,l) depth profile of ^{7}Li fraction.

6. Neutron reflectometry data and error analysis

This section describes how Li permeation parameters (time constant of the Li permeation process and Li permeability) were obtained from in-situ NR experiments.

Fitting of the experimental NR patterns with a layer model using Parratt32 give neutron SLD, thickness and roughness of the individual layers. Table 1 lists the results for the as-deposited MLs (Figure 1 of the main article).

Table S1. Parameters used for the simulation of the reflectivity pattern presented in Figure 1 of the main article. The upper (lower) half of the table lists the parameters presented in Figure 1a (1c). Five [$^6LiNbO_3$ / Si / $^7LiNbO_3$ / Si] four layer units are deposited on a Si wafer and capped by a $^6LiNbO_3$ layer (see Figure S1). The layers termed $^7LiNbO_3$ and $^6LiNbO_3$ have a ^6Li and ^7Li isotope concentration of $^7Li_{0.90}Li_{0.10}$ and $^7Li_{0.10}{}^6Li_{0.90}$, respectively, as measured by SIMS (Figure S4). Error limits correspond to a 10% increase of χ^2 of the best fit with respect to the fitted parameter only [S12].

see Figure 1a of the article:	layer	SLD (10^{-6} Å^{-2})	thickness (nm)	roughness (nm)
air	air	0	--	--
capping-layer	$^6LiNbO_3$	4.14 ± 0.4	10.0 ± 0.8	2.1 ± 0.4
5 × the four layer pack Si/$^{nat}LiNbO_3$/Si/$^6LiNbO_3$	Si	1.9 ± 0.1	14 ± 0.2	1.2 ± 0.5
	$^7LiNbO_3$	3.84 ± 0.05	10 ± 0.2	1.2 ± 0.5
	Si	1.9 ± 0.1	14 ± 0.2	1.2 ± 0.5
	$^6LiNbO_3$	4.48 ± 0.05	10 ± 0.2	1.2 ± 0.5
Si-wafer	Si	2.07	--	1.7
see Figure1c of the article:	layer	SLD (10^{-6} Å^{-2})	thickness (nm)	roughness (nm)
air	air	0	--	--
capping-layer	$^6LiNbO_3$	4.1 ± 0.3	10 ± 0.9	2.6 ± 0.7
5 × the four layer pack Si/$^{nat}LiNbO_3$/Si/$^6LiNbO_3$	Si	1.9 ± 0.1	22 ± 0.2	1.4 ± 0.5
	$^7LiNbO_3$	3.83 ± 0.05	8 ± 0.2	1.4 ± 0.5
	Si	1.9 ± 0.1	22 ± 0.2	1.4 ± 0.5
	$^6LiNbO_3$	4.48 ± 0.05	8 ± 0.2	1.4 ± 0.5
Si-wafer	Si	2.07	--	0.5

The quantity of interest is the Li permeability, which is expressed as

$$P = S \cdot D \tag{S1}$$

where S is the Li solubility and D is the Li diffusivity. It was determined from the time constant (τ) governing the Li isotope intermixing process which is occurring by Li permeation through the Si layers. The decrease of the Li isotope contrast in the Li reservoirs is regulated by the following exponential decay (see the SI of reference [S5])

$$K(t) = \frac{f(t) - f_{min}}{f_{max} - f_{min}} = \exp\left(-\frac{t}{\tau} \right) \tag{S2}$$

where f_{max} and f_{min} are the ^{6}Li (^{7}Li) isotope fraction in the $^6LiNbO_3$ ($^7LiNbO_3$) reservoirs in the as-deposited state and after complete Li isotope intermixing, respectively. f(t) is the Li fraction as a function of annealing time. The parameter τ represents the time constant of Li contrast decrease. Finally, the Li permeability is given by the time constant of Li isotope intermixing process (see SI of reference [S5]) according to

$$P = \frac{1}{4} \cdot \frac{M_{Si}}{M_{LiNbO3}} \cdot \frac{\rho_{LiNbO3}}{\rho_{Si}} \cdot \frac{d_{LiNbO3} \cdot d_{Si}}{\tau} \qquad \text{(S3)}$$

where M_{Si} = 28.09 g/mol is the molar mass of Si, M_{LiNbO3} = 147 g/mol is the molar mass of $LiNbO_3$, ρ_{LiNbO3} = (4 ± 0.1) g/cm^3 is the mass density of the $LiNbO_3$ layer, ρ_{Si} = (2 ± 0.1) g/cm^3 is the mass density of the Si layer, d_{Si} is the thickness of the Si layer, and d_{LiNbO3} is the thickness of the $LiNbO_3$ reservoir layer. These parameters were obtained from fits to measured NR curves (and using reference [S11]). So, the main issue for Li permeability calculation is to determine the time constant τ of the Li permeation process from the in-situ NR experiments done in this study.

Figure S5a,c present measured NR patterns from the as-deposited MLs (circles) together with NR simulations (red lines). The NR simulations here were performed without Li isotope contrast in the MLs which is evidenced in Figure S5b,d by a lack of contrast in the neutron scattering length density (SLD) of the Li reservoir layers ($LiNbO_3$). Consequently, the half order Bragg reflections (in literature many authors use the term 'Bragg peak'; in fact, 'reflections' is a more suitable term) are not present in this simulation (Figure S5a,c) as expected.

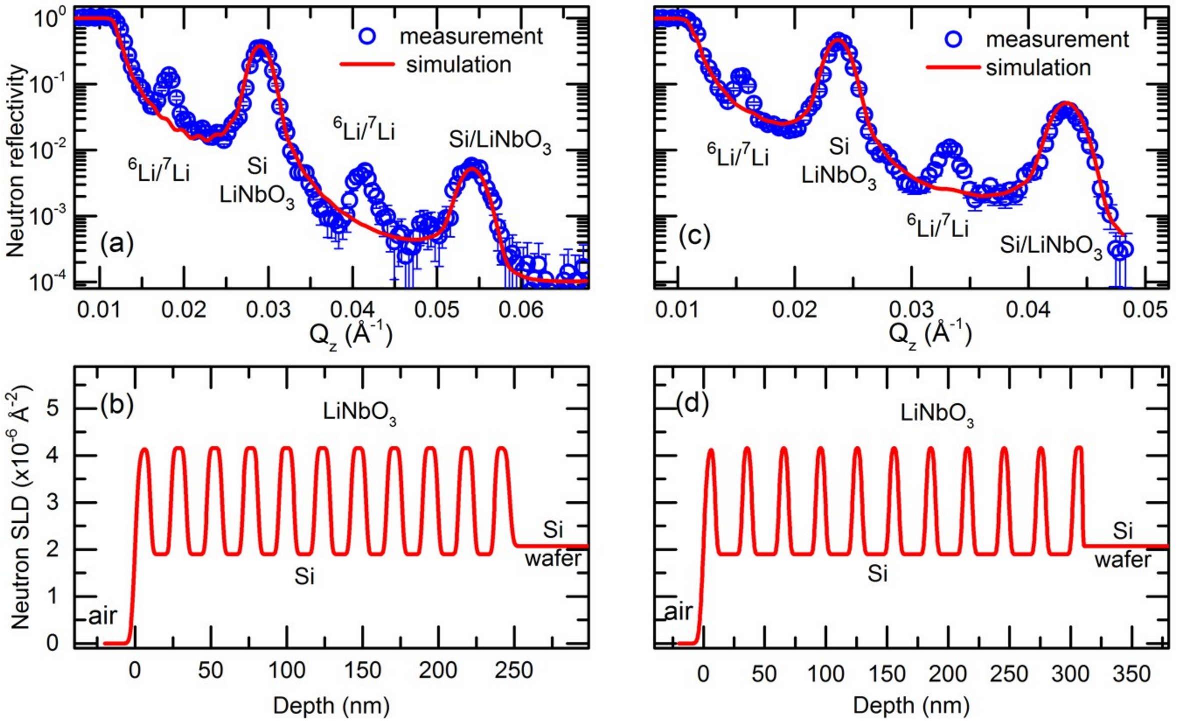

Figure S5. (a,c) Measured NR pattern (open symbols) for the multilayer with (a) 14 nm and (c) 22 nm thin Si intermediary layers in the as-deposited state. NR simulations (lines) performed without Li isotope contrast between the Li reservoir layers. (b,d) Neutron scattering length density depth profiles for lack of Li isotope contrast between the Li reservoir layers.

Figure S6 and S7 present NR simulations performed to investigate the influence of Li isotope contrast K in MLs with 14 nm (Figure S6) and 22 nm (Figure S7) thin Si intermediary layers. The panels (c) in Figures S6 and S7 present results of calculations which reveal that there is, as expected, a linear dependence of neutron SLD on the Li isotope fraction in the Li reservoir layer.

The decline of the Li isotope contrast is reflected only in the intensity of the half order Bragg reflections (Figure S6 and S7). The panels (b) of Figures S6 and S7 presents the background corrected NR data which are obtained by subtracting the simulated NR curve for full Li isotope intermixing ($R_{intermixed}$, i.e., for K = 0 and $\Delta\rho = 0$) from each simulated NR curve (R) and dividing this entity by the simulated NR curve of full Li isotope intermixing, according to

$$\frac{R - R_{intermixed}}{R_{intermixed}} \quad . \tag{S4}$$

The area (A) of the background corrected Bragg reflections given in Figures S6b and S7b is considered in the following to be the intensity of the Bragg reflections. The panel (d) of Figures S6 and S7 presents the intensity of the half order Bragg reflections of dependence on the Li isotope contrast K. Both entities, i.e. A and K, are given in Figures 6 and 7 in percentage, according to

$$A^{\%} = \frac{A}{\max(A)} \cdot 100\ \% \quad , \quad K^{\%} = \frac{K}{\max(K)} \cdot 100\ \% \quad . \tag{S5}$$

Figures S6d and S7d show that the dependence of the Bragg reflections intensity on the Li isotope contrast, i.e., the A(K) dependence, is not linear. A parabolic behavior is expected from kinematic scattering theory (consideration of single reflections). This is not the case for the calculated A(K) dependence (Figure S6 d and S7 d), because the NR simulation were performed according to the Parratt formalism of multiple reflections, i.e., taking into account the dynamic scattering theory.

The calculated A(K) dependence can be well fitted with a second order polynomial

$$A = b \cdot K + c \cdot K^2 \tag{S6}$$

where b and c are fit parameters. Table S2 lists the fit parameters and their error limits obtained from the NR simulations of the MLs with 14, 17 and 22 nm thin Si intermediary layers.

Table S2. Parameters b and c and their error limits obtained from a polynomial fit ($A = bK + cK^2$, see Figures S6 d and S7 d) to the curve: half order Bragg reflections area (A) vs. Li isotope contrast (K) for different Si intermediary layers.

Thickness of Si intermediary layers	b	error (Δb/b)	c	error (Δc/c)
14 nm	0.578	1.7 %	0.0043	2.3 %
17 nm	0.530	1.9 %	0.0047	2.8 %
22 nm	0.483	0.6 %	0.0052	1.0 %

Hence, from Equation (S6), the Li isotope contrast (K) can be calculated easily from the experimentally determined intensity of the half order neutron Bragg reflections (A) according to

$$K = \frac{-b + \sqrt{b^2 + 4 \cdot c \cdot A}}{2 \cdot c} \tag{S7}$$

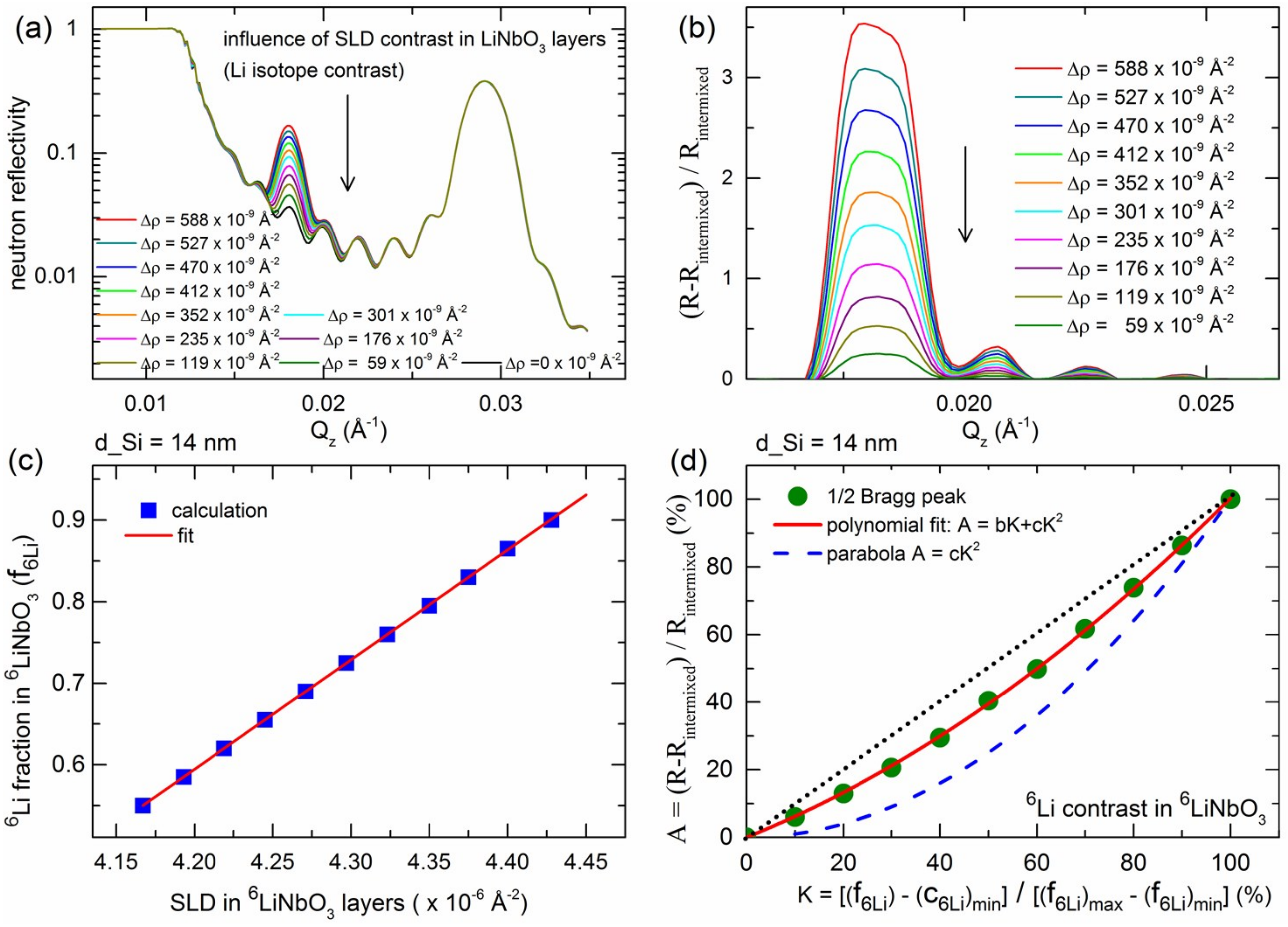

Figure S6. NR simulations of the multilayer with 14 nm thin Si intermediary layers. (a) Simulated NR patterns for different neutron scattering length density (SLD) differences between the $LiNbO_3$ layers. (b) The influence of the SLD difference between the Li isotope reservoirs on the NR curve as expressed by (S4). (c) Calculated linear dependence of the Li isotope fraction on the SLD, f = f(SLD). (d) Calculated dependence of the Li isotope induced half order Bragg reflections intensity on the Li isotope contrast A = A(K) (Equation (S6)).

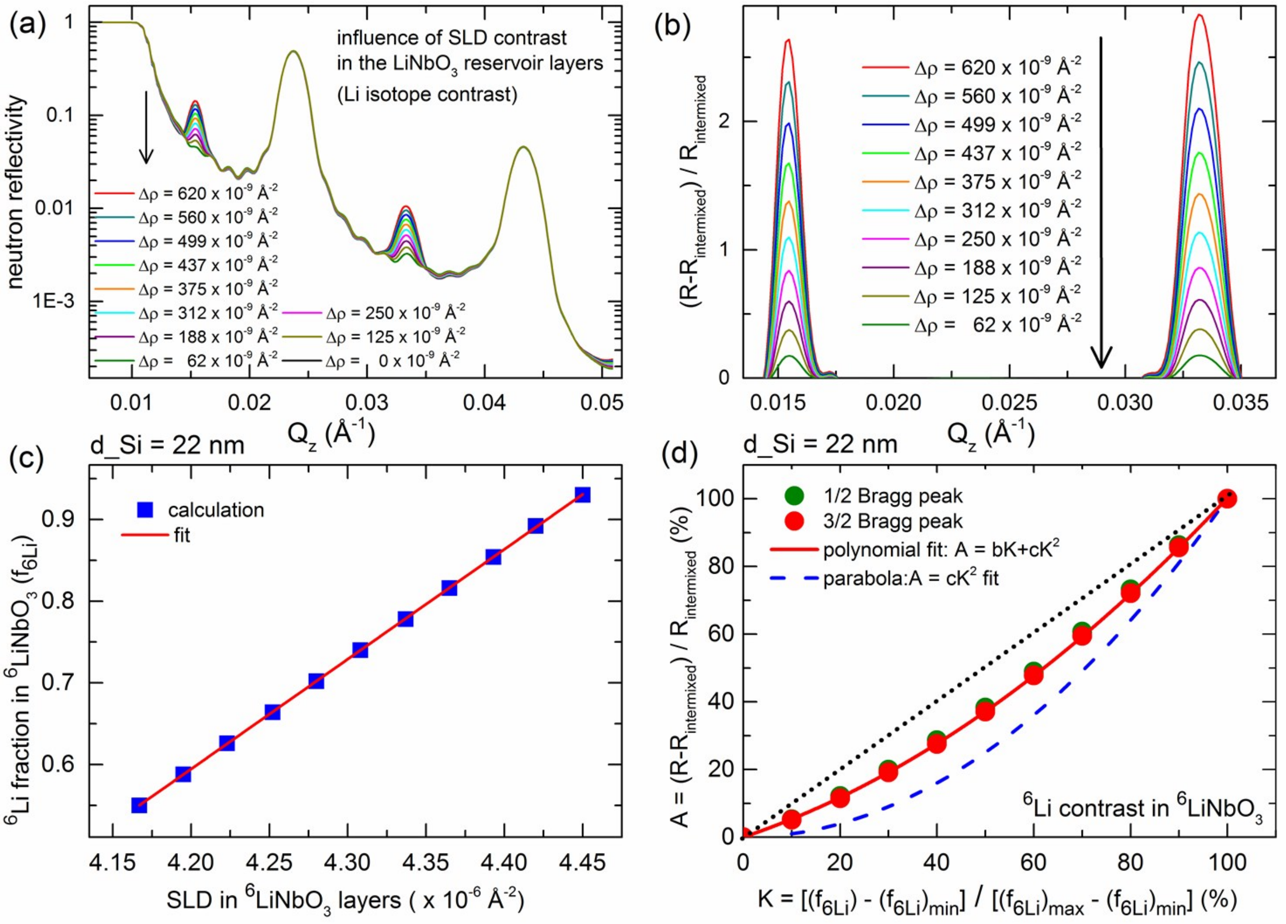

Figure S7. NR simulations of the multilayer with 22 nm thin Si intermediary layers. (a) Simulated NR patterns for different neutron scattering length density (SLD) differences between the $LiNbO_3$ layers. (b) The influence of the SLD difference between the Li isotope reservoirs on the NR curve as expressed by (S4). (c) Calculated linear dependence of the Li isotope fraction on the SLD, f = f(SLD). (d) Calculated dependence of the Li isotope induced half order Bragg reflections intensity on the Li isotope contrast A = A(K) (Equation (S6)).

Figure S8 presents the half order Bragg peaks after background subtraction for NR patterns measured in-situ at different temperatures. The Bragg reflections were fitted with a Gaussian function. The area of Gaussian function and its errors are taken to be the Bragg reflections intensity and the error of Bragg reflections intensity, respectively. Figure S9 presents the normalized intensity of the Bragg reflections, i.e., A/max(A), together with the error limits of dependence on annealing time at different temperatures for the MLs studied in this work. Consequently, all quantities on the right side of Equation (S7), i.e., (b, c, A) have calculable errors and in that way the error of the Li isotope contrast can also be calculated. The error of b and c is obtained from the polynomial fit to the NR simulation results given in Figures S6 and S7 (Table S2). The errors of A are, as mentioned, obtained by the Gaussian fit of the background corrected in-situ measured half order Bragg reflections.

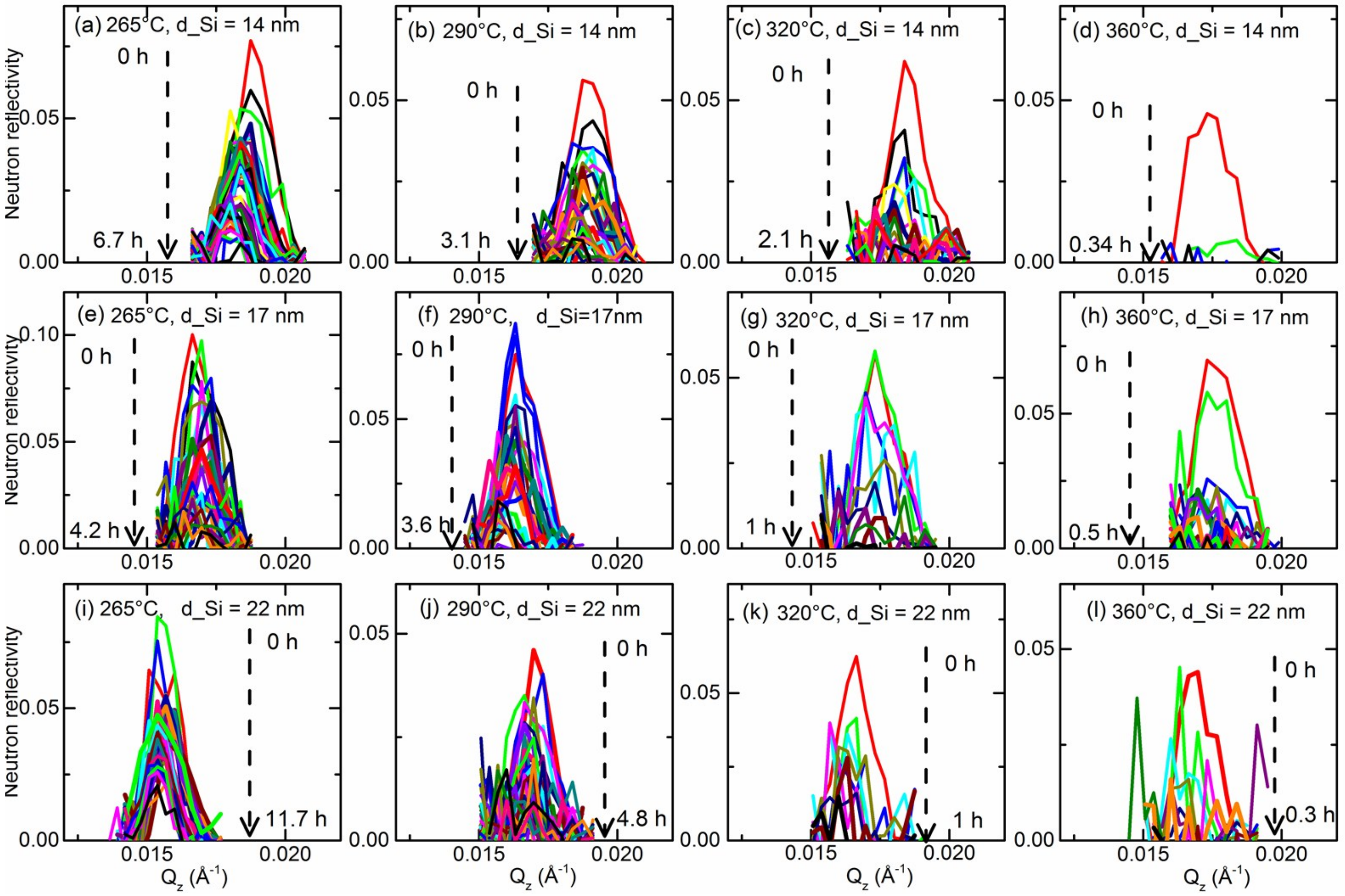

Figure S8. Half order Bragg reflections after subtracting the background as obtained from the in-situ experiments. The Bragg reflections were recorded while Li permeation takes place at (a,e,i) 265 °C (538 K), (b,f,j) 290 °C (563 K), (c,g,k) 320 °C (593 K) and (d,h,l) 360 °C (633 K). The thickness of the Si layers is given in the legend.

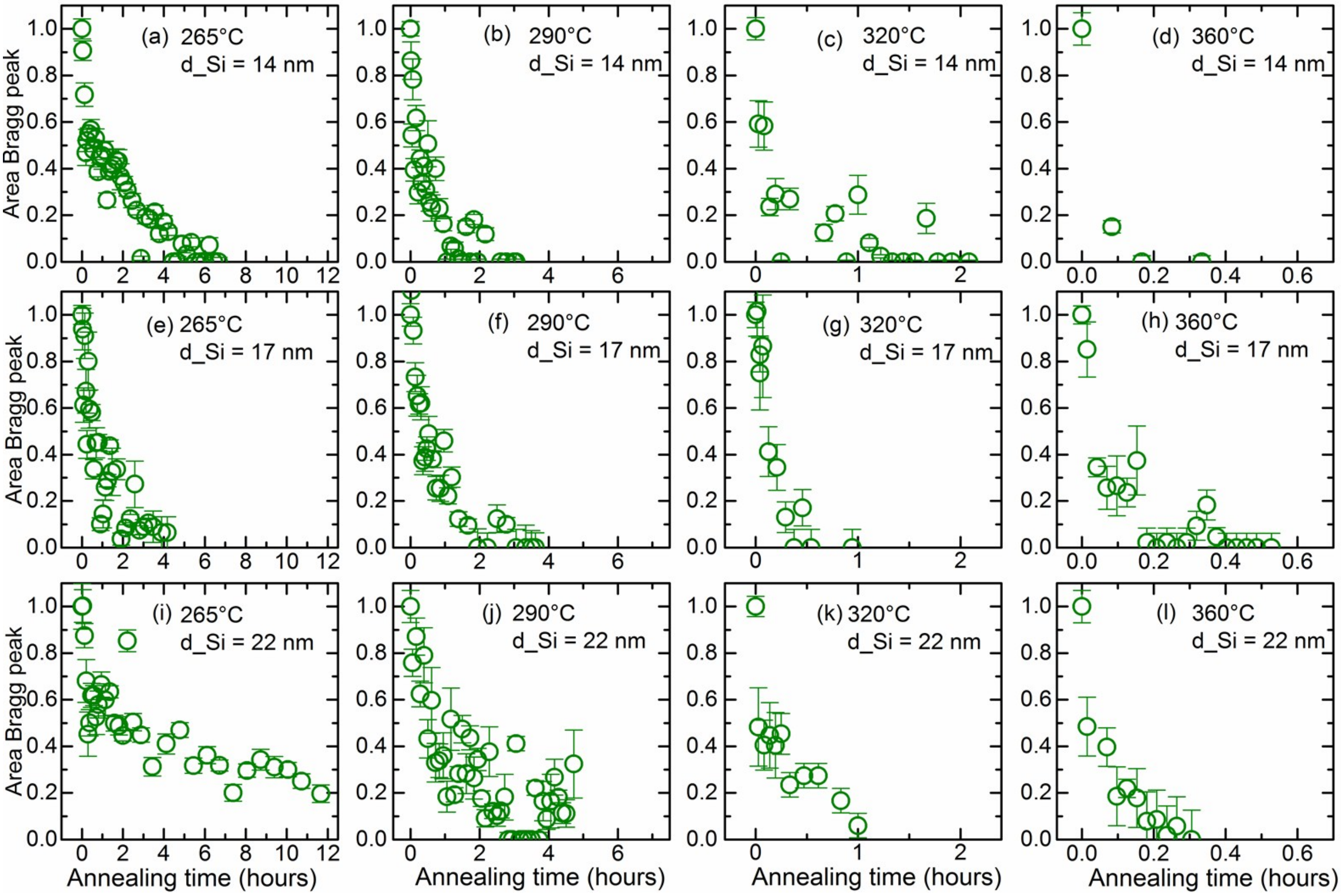

Figure S9. Change of the normalized intensity (A/max(A)) of the half order NR Bragg reflections measured during Li permeation at (a,e,i) 265°C (538 K), (b,f,j) 290°C (563 K), (c,g,k) 320°C (593 K) and (d,h,l) 360°C (633 K). The thickness of the Si layers is given in the legend.

If the variables (b,c,A) are independent from each other, then the error in Li isotope contrast can be calculated from the error propagation law according to

$$\frac{\Delta K}{K}=\frac{1}{K}\cdot\sqrt{\left(\frac{\partial K}{\partial b}\cdot\Delta b\right)^2+\left(\frac{\partial K}{\partial c}\cdot\Delta c\right)^2+\left(\frac{\partial K}{\partial A}\cdot\Delta A\right)^2}\quad\Rightarrow$$

(S8)

$$\frac{\Delta K}{K}=\frac{1}{\sqrt{b^2+4\cdot c\cdot A}}\cdot\sqrt{\left[b\cdot\left(\frac{\Delta b}{b}\right)\right]^2+\left[\left(\sqrt{b^2+4\cdot c\cdot A}-\frac{A}{K}\right)\cdot\left(\frac{\Delta c}{c}\right)\right]^2+\left[\frac{A}{K}\cdot\left(\frac{\Delta A}{A}\right)\right]^2}$$

The variables b and c are obtained from the polynomial fit of Equation (S6) (Figures S6 and S7, Table S2) and are not independent from each other. In that case, the error of the Li isotope contrast can be calculated as

$$\frac{\Delta K}{K}=\frac{1}{K}\cdot\sqrt{\left(\left|\frac{\partial K}{\partial b}\cdot\Delta b\right|+\left|\frac{\partial K}{\partial c}\cdot\Delta c\right|\right)^2+\left(\frac{\partial K}{\partial A}\cdot\Delta A\right)^2}\quad\Rightarrow$$

(S9)

$$\frac{\Delta K}{K}=\frac{1}{\sqrt{b^2+4\cdot c\cdot A}}\cdot\sqrt{\left[\left|b\cdot\left(\frac{\Delta b}{b}\right)\right|+\left|\left(\sqrt{b^2+4\cdot c\cdot A}-\frac{A}{K}\right)\cdot\left(\frac{\Delta c}{c}\right)\right|\right]^2+\left[\frac{A}{K}\cdot\left(\frac{\Delta A}{A}\right)\right]^2}$$

The error limits obtained by formula (S9) are presented in Figure 3 of the main article.

Finally, if all variables would be dependent on each other, the error in Li contrast is largest and is given by

$$\frac{\Delta K}{K} = \frac{1}{K}\cdot\left(\left|\frac{\partial K}{\partial b}\cdot\Delta b\right| + \left|\frac{\partial K}{\partial c}\cdot\Delta c\right| + \left|\frac{\partial K}{\partial A}\cdot\Delta A\right|\right) \quad \Rightarrow \tag{S10}$$

$$\frac{\Delta K}{K} = \frac{1}{\sqrt{b^2+4\cdot c\cdot A}}\cdot\left[\left|b\cdot\left(\frac{\Delta b}{b}\right)\right| + \left|\left(\sqrt{b^2+4\cdot c\cdot A}-\frac{A}{K}\right)\cdot\left(\frac{\Delta c}{c}\right)\right| + \left|\frac{A}{K}\cdot\left(\frac{\Delta A}{A}\right)\right|\right]$$

Figure S10, S11 and S12 presents the annealing time dependence of Li isotope contrast at different temperatures for the MLs studied in this work with errors calculated according to Equation (S8), (S9) and (S10), respectively.

The lines in Figure S10, S11 and S12 represent the fit of the contrast K(t) with the exponential decay function given in Equation (S2). The obtained time constants of Li permeation process are listed in Table S3. The time constants (for same temperature and same ML) are identical within error limits, independently from the manner of error limit allocation to the Li isotope contrast.

Table S3. Time constants of the Li permeation process as experimentally obtained from the Li isotope contrast decrease presented in Figures S10, S11 and S12 using different error calculations together with annealing temperature, and thicknesses.

temperature	thickness Si layer (nm)	thickness $LiNbO_3$ layer (nm)	time constant τ (hours) using error (S8)	time constant τ (hours) using error (S9)	time constant τ (hours) using error (S10)
265°C	14 ± 1	10 ± 1	1.78 ± 0.11	1.69 ± 0.11	1.78 ± 0.13
265°C	17 ± 1	10 ± 1	1.68 ± 0.12	1.66 ± 0.13	1.84 ± 0.18
265°C	22 ± 1	8 ± 1	7.08 ± 0.70	7.71 ± 0.70	6.80 ± 0.70
290°C	14 ± 1	10 ± 1	0.52 ± 0.05	0.53 ± 0.05	0.49 ± 0.06
290°C	17 ± 1	10 ± 1	0.91 ± 0.06	0.87 ± 0.06	0.89 ± 0.07
290°C	22 ± 1	8 ± 1	1.73 ± 0.13	1.67 ± 0.13	1.76 ± 0.14
320°C	14 ± 1	10 ± 1	0.22 ± 0.05	0.28 ± 0.05	0.19 ± 0.04
320°C	17 ± 1	10 ± 1	0.22 ± 0.05	0.22 ± 0.05	0.24 ± 0.03
320°C	22 ± 1	8 ± 1	0.51 ± 0.01	0.48 ± 0.06	0.46 ± 0.07
360°C	14 ± 1	10 ± 1	0.052 ± 0.004	0.056 ± 0.004	0.051 ± 0.005
360°C	17 ± 1	10 ± 1	0.071 ± 0.01	0.087 ± 0.01	0.072 ± 0.01
360°C	22 ± 1	8 ± 1	0.15 ± 0.04	0.13 ± 0.03	0.16 ± 0.07

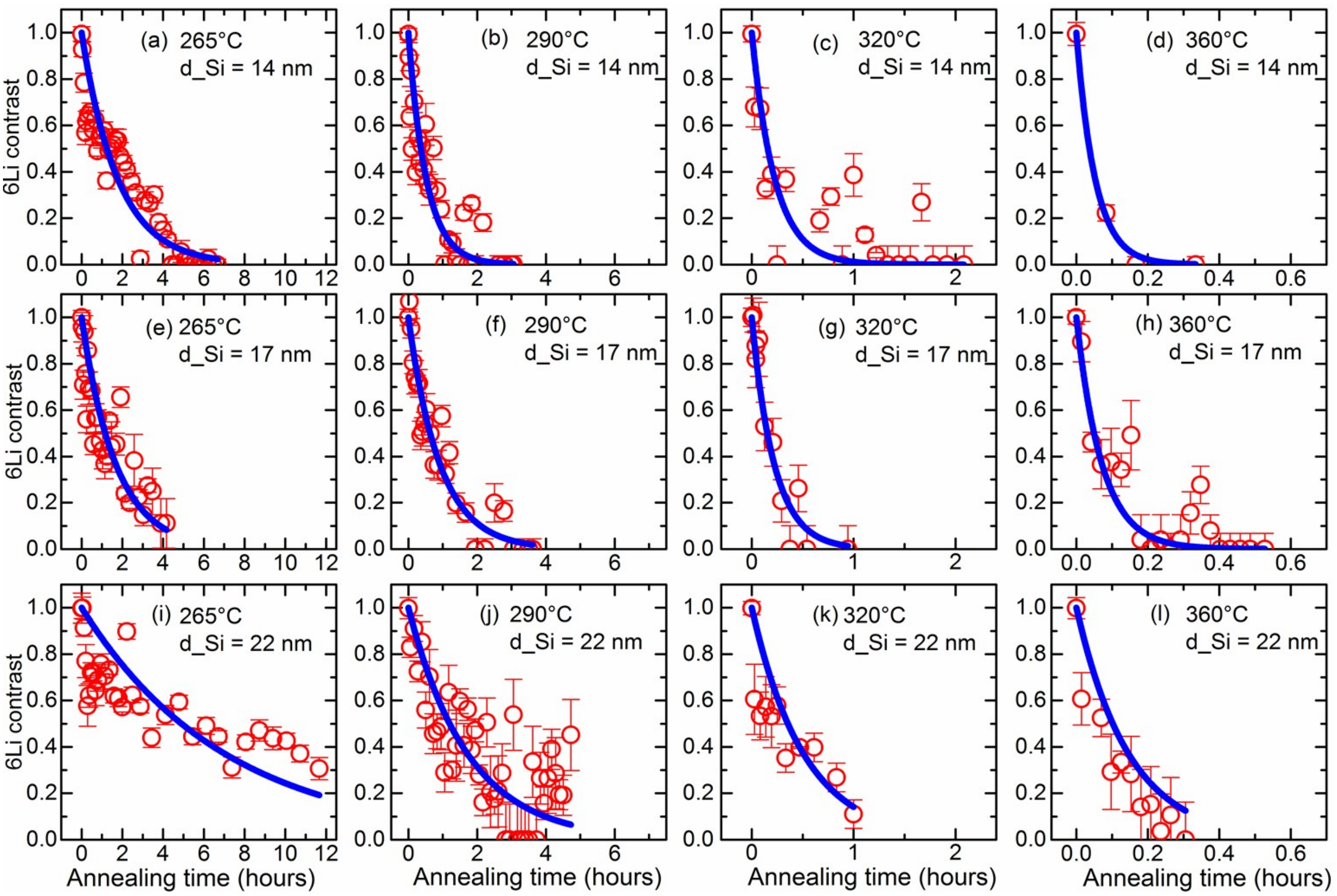

Figure S10. Annealing time behavior of the ^{6}Li contrast K in the ^{6}Li reservoir layers obtained from in-situ NR measurements during Li permeation through the Si layer of different thickness at different temperatures. The error of Li isotope contrast was obtained according to Equation (S8). Lines correspond to the fit with the exponential decay function given in Equation (S2).

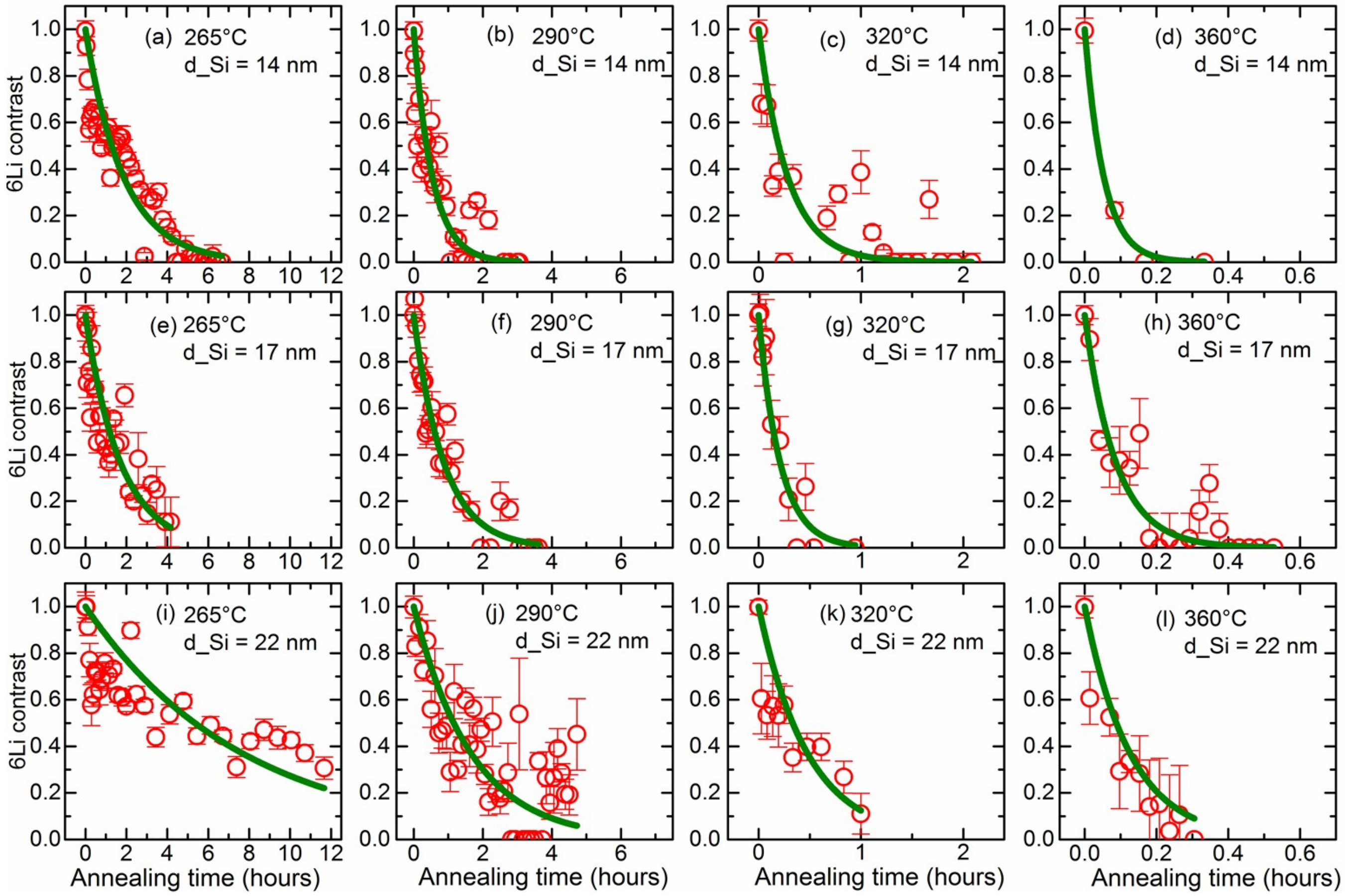

Figure S11. Annealing time behavior of the ^{6}Li contrast K in the ^{6}Li reservoir layers obtained from in-situ NR measurements during Li permeation through the Si layer of different thickness at different temperatures. The error of Li isotope contrast was obtained according to Equation (S9). Lines correspond to the fit with the exponential decay function given in Equation (S2).

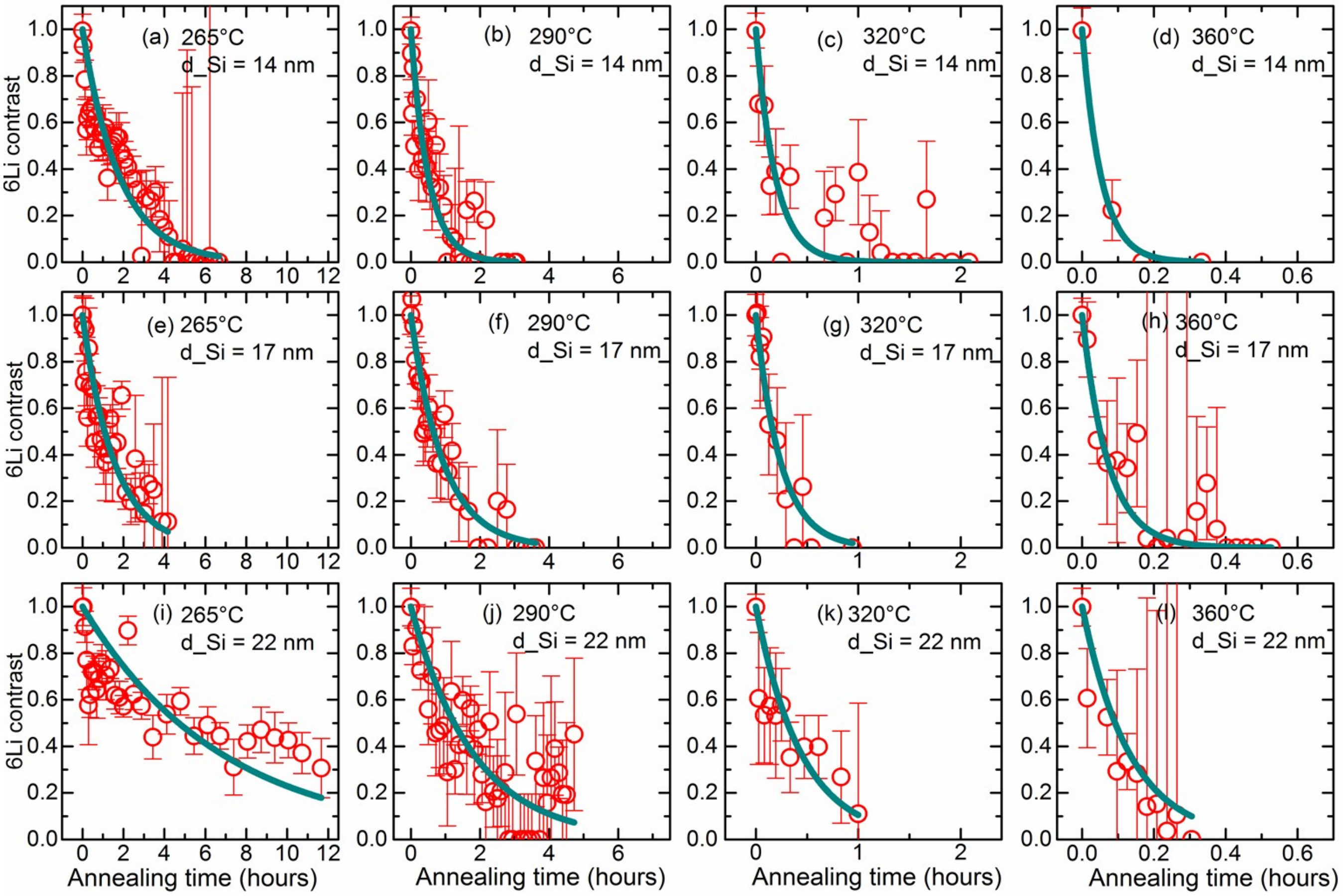

Figure S12. Annealing time behavior of the ^{6}Li contrast K in the ^{6}Li reservoir layers obtained from in-situ NR measurements during Li permeation through the Si layer of different thickness at different temperatures. The error of Li isotope contrast was obtained according to Equation (S10). Lines correspond to the fit with the exponential decay function given in Equation (S2).

The error limits of the Li permeabilities (P) are calculated according to the error propagation law.

If the values on the right side of Equation (S3) are independent from each other, then the error of the Li permeability is given by

$$\Delta P = \sqrt{\begin{aligned}&\left(\frac{\partial P}{\partial \rho_{\mathrm{LiNbO3}}}\right)^2 \cdot (\Delta\rho_{\mathrm{LiNbO3}})^2 + \left(\frac{\partial P}{\partial \rho_{\mathrm{Si}}}\right)^2 \cdot (\Delta\rho_{\mathrm{Si}})^2 + \\ &+ \left(\frac{\partial P}{\partial d_{\mathrm{LiNbO3}}}\right)^2 \cdot (\Delta d_{\mathrm{LiNbO3}})^2 + \left(\frac{\partial P}{\partial d_{\mathrm{Si}}}\right)^2 \cdot (\Delta d_{\mathrm{Si}})^2 + \\ &+ \left(\frac{\partial P}{\partial \tau}\right)^2 \cdot (\Delta\tau)^2\end{aligned}} \qquad \text{(S11)}$$

Using Equation (S3) one obtains

$$\frac{\Delta P}{P} = \sqrt{\left(\frac{\Delta\rho_{\mathrm{LiNbO3}}}{\rho_{\mathrm{LiNbO3}}}\right)^2 + \left(\frac{\Delta\rho_{\mathrm{Si}}}{\rho_{\mathrm{Si}}}\right)^2 + \left(\frac{\Delta d_{\mathrm{LiNbO3}}}{d_{\mathrm{LiNbO3}}}\right)^2 + \left(\frac{\Delta d_{\mathrm{Si}}}{d_{\mathrm{Si}}}\right)^2 + \left(\frac{\Delta\tau}{\tau}\right)^2} \;. \qquad \text{(S12)}$$

Obviously, the time constant of Li contrast decrease, τ, depends on the Si and $LiNbO_3$ layer thickness and is not independent. In that case, the error of the Li permeability can be given by

$$\frac{\Delta P}{P} = \left|\frac{\Delta \tau}{\tau}\right| + \sqrt{\left(\frac{\Delta \rho_{LiNbO3}}{\rho_{LiNbO3}}\right)^2 + \left(\frac{\Delta \rho_{Si}}{\rho_{Si}}\right)^2 + \left(\frac{\Delta d_{LiNbO3}}{d_{LiNbO3}}\right)^2 + \left(\frac{\Delta d_{Si}}{d_{Si}}\right)^2} \qquad \text{(S13)}$$

The error of mass densities amounts to ~ 5 %. Table S4 lists the temperature of the Li permeation process, the layer thicknesses, and the Li permeability with error limits as calculated according to Equation (S12) and (S13). The larger errors calculated with formula (S13) were used for further analysis in the main article.

Table S4. Li permeabilities with error limits calculated according to Equation (S12) and (S13). Also given are annealing temperature as well as Si layer and $LiNbO_3$ layer thickness.

temperature	thickness Si layer (nm)	thickness $LiNbO_3$ layer (nm)	Li permeability (m^2/s) with error limits given by (S12)	Li permeability (m^2/s) with error limits given by (S13)
265°C	14 ± 1	10 ± 1	(1.9 ± 0.2)×E-21	(1.8 ± 0.3)×E-21
265°C	17 ± 1	10 ± 1	(2.5 ± 0.3)×E-21	(2.4 ± 0.4)×E-21
265°C	22 ± 1	8 ± 1	(7.3 ± 0.9)×E-22	(7.3 ± 1.3)×E-21
290°C	14 ± 1	10 ± 1	(6.5 ± 0.8)×E-21	(6.5 ± 1.1)×E-21
290°C	17 ± 1	10 ± 1	(4.5 ± 0.5)×E-21	(4.5 ± 0.7)×E-21
290°C	22 ± 1	8 ± 1	(2.2 ± 0.3)×E-22	(2.2 ± 0.4)×E-21
320°C	14 ± 1	10 ± 1	(1.9 ± 0.4)×E-20	(1.9 ± 0.6)×E-20
320°C	17 ± 1	10 ± 1	(1.6 ± 0.3)×E-20	(1.6 ± 0.4)×E-20
320°C	22 ± 1	8 ± 1	(9.0 ± 1.6)×E-21	(9.0 ± 2.2)×E-21
360°C	14 ± 1	10 ± 1	(7.5 ± 0.8)×E-20	(7.5 ± 1.1)×E-20
360°C	17 ± 1	10 ± 1	(5.7 ± 0.5)×E-20	(5.7 ± 0.6)×E-20
360°C	22 ± 1	8 ± 1	(3.0 ± 0.9)×E-20	(3.0 ± 1.2)×E-20

The permeabilities follow the Arrhenius law

$$P = P_0 \exp(-\Delta H/kT) \qquad \text{(S14)}$$

where ΔH and P_0 are the activation enthalpy of Li permeation process and the pre-exponential factor, respectively.

ΔH and P_0 obtained from the in-situ NR experiments are listed in Table S5.

Table S5. Activation enthalpy (ΔH) and pre-exponential factor (P_0) for different Si thicknesses as obtained from fitting the experimentally determined permeabilities to the Arrhenius law (Equation S14).

Thickness of Si layer	ΔH (eV)	$\log_{10} P_0$ (log(m^2/s))
14 nm	1.14 ± 0.04	-10.0 ± 0.3
17 nm	1.00 ± 0.08	-11.2 ± 0.7
22 nm	1.20 ± 0.06	-9.9 ± 0.5

7. Diffusion rates at the interface

The time constant (τ) of the Li permeation experiment describes the transport through both, the $LiNbO_3$/Si interface and the Si layer. Since this time constant was measured as a function of thickness of the Si layer, it should be possible to determine separately the time constant of the Li transport process through the $LiNbO_3$/Si interface. This would enable to make some predictions at what thickness of the Si layer the transport through the interface becomes significant for the overall process. As described in references [S5 S6], Li diffusivities in the Li reservoir are several orders of magnitudes faster than those in silicon and consequently this quantity can be neglected in the following considerations.

For the one-dimensional case, the time interval needed for one Li atom to reach the other Li reservoir by diffusion through Si and the interfaces is given by the sum of the time interval needed for Li to cross the interfaces ($t_{interface}$) and the time interval needed for Li to diffuse through the silicon layer ($d_{Si}^2/2D$) (left side of equation S15). A link between these time intervals and the measured time constant of the Li permeation experiments, τ, has to be found. The sum ($t_{interface} + d_{Si}^2/2D$) is independent from the amount of Li in the Li reservoirs, i.e., independent from the $LiNbO_3$ layer thickness. On the other hand, the time constant, τ, measured in Li permeation experiments depends on the $LiNbO_3$ layer thickness. For example, τ should be 10 times larger if 100 nm instead of 10 nm thin $LiNbO_3$ layers are used as Li reservoirs [ref. S1, S5]. Hence, the time constant, τ, has to be transformed into a time constant which is independent from the $LiNbO_3$ thickness according to the following considerations:

The layer thickness of $LiNbO_3$ is equal to the product between the number density of the Li atomic planes ($N_{Li\text{-}atomic\text{-}planes}$) parallel to the surface and the interlayer distance ($d_{Li\text{-}interlayer\text{-}distance}$) between such two adjacent Li atomic planes. The latter quantity is assessed to $d_{Li\text{-}interlayer\text{-}distance} \approx 0.3$ nm. Dividing now the time constant, τ, of the Li permeation process by $N_{Li\text{-}atomic\text{-}planes}$ we get a quantity that is independent of the $LiNbO_3$ layer thickness. It represents the time interval which is necessary for a number of Li atoms corresponding to one Li atomic plane to cross the interface and to diffuse through the silicon layer. Finally, we get

$$t_{\mathrm{interface}} + \frac{d_{\mathrm{Si}}^2}{2D} = \frac{\tau}{N_{\mathrm{Li-atomic-planes}}} = \frac{\tau}{\dfrac{d_{\mathrm{LiNbO3}}}{d_{\mathrm{Li-interlayer-distance}}}} \approx \frac{\tau}{\dfrac{d_{\mathrm{LiNbO3}}}{0.3\,\mathrm{nm}}} \qquad \text{(S15)}$$

where d_{Si} is the Si layer thickness, D is the Li diffusion coefficient in silicon, $N_{Li\text{-}atomic\text{-}planes}$ is the number of Li atomic planes in a $LiNbO_3$ layer parallel to the surface, d_{LiNbO3} is the $LiNbO_3$ layer thickness and $d_{Li\text{-}interlayer\text{-}distance}$ is the approximate interlayer distance between the Li layers.

All values on the right side of equation S15, i.e., τ and d_{LiNBO3}, are known. Figure S13 presents the right side of equation S15 plotted of dependence on the Si layer thickness for different temperatures as determined from the Li permeation experiments. A fit of the parabola given on the left side of equation S15 to the data of Figure S13 delivers the time interval $t_{interface}$ and the diffusion coefficients of Li in the Si layers. A constraint of non-negative time intervals was imposed on the fits. $t_{interface}$ is obtained to be virtually zero. This illustrates that Li diffusion through the $LiNbO_3$/Si interface is found to be extremely fast. The Li transport through this interface becomes relevant for the overall transport process if the following condition is fulfilled

$$t_{\mathrm{int}erface} = \frac{d_{Si}^{*\,2}}{2D} \quad \Rightarrow \quad d_{Si}^{*} = \sqrt{2Dt_{\mathrm{int}erface}} \qquad \text{(S16)}$$

Hence, the corresponding critical Si thickness d_{Si}* is also zero. Consequently, Li diffusion in silicon and not Li diffusion through the interface is the rate determining step of the Li transport process for all relevant Si layer thicknesses.

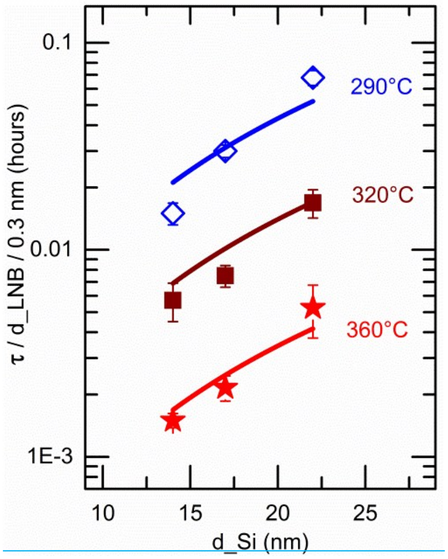

Fig. S13. Ratio of the time constant of Li permeation (τ) divided by number of Li atomic planes (d_LNB/0.3nm) in the Li reservoir (the right side of equation S15), as a function of Si layer thickness d_Si investigated in this work at different temperatures.

8. References

[S1] E. Hüger, L. Dörrer, J. Rahn, T. Panzner, J. Stahn, G. Lilienkamp and H. Schmidt, *Nano Lett*., 2013, **13**, 1237.

[S2] E. Hüger, L. Dörrer, J. Stahn, T. Geue and H. Schmidt, *Defect Diffus. Forum,* 2015, **363**, 49.

[S3] E. Hüger, J. Stahn and H. Schmidt, *J. Electrochem. Soc*., 2015, **162**, A7104.

[S4] F. Strauß, E. Hüger, P. Heitjans, T. Geue, J. Stahn and H. Schmidt, *Energy Technology,* 2016, **12**, 1582.

[S5] E. Hüger, L. Dörrer and H. Schmidt, *Chem. Mater*., 2018, **30**, 3254.

[S6] E. Hüger, L. Dörrer, R. Yimnirun, J. Jutimoosik, J. Stahn and A. Paul, *PCCP,* 2018, **20**, 23233.

[S7] E. Hüger and H. Schmidt, *J. Phys. Chem. C,* 2018, **122**, 28528.

[S8] F. Strauß, E. Hüger, P. Heitjans, V. Trouillet, M. Bruns and H. Schmidt, *RSC Adv.,* 2015, **5**, 7192.

[S9] J. Rahn, E. Hüger, L. Dörrer, B. Ruprecht, P. Heitjans and H. Schmidt, *Z. Phys. Chem*., 2012, **226**, 439.

[S10] C. Braun, Parratt32 or the reflectometry tool, HMI, Berlin, [http://www.helmholtz-berlin.de].

[S11] See [http://www.ncnrs.nist.gov/resources/sldcalc.html].

[S12] B. Jerliu, L. Dörrer, E. Hüger, G. Borchardt, R. Steitz, U. Geckle, V. Oberst, M. Bruns, O. Schneider and H. Schmidt, *PCCP,* 2013, **15**, 7777.